ACS APPLIED NANO MATERIALS

www.acsanm.org Article

Polar Cubic CeO_2 Nanoparticles on Graphene for Enhanced Room-Temperature NO_2 Sensing Performance

Lizhai Zhang, Huiyan Xu, Yuhong Huang, Hongbing Lu, Taotao Ai,* Kewei Xu, Fei Ma,* and Paul K. Chu*

Cite This: *ACS Appl. Nano Mater.* 2023, 6, 10551−10558 Read Online

ACCESS | Metrics & More | Article Recommendations | Supporting Information

ABSTRACT: Composites of graphene and CeO_2 nanoparticles with high-energy {100} facets exposed are prepared by the hydrothermal method. The percentage of high-energy {100} polar plane increases with elevating temperature, but the proportion of Ce^{3+} and oxygen vacancy (O_v) decreases. As a result, the sensitivity of CeO_2{100}/graphene composites toward NO_2 at room temperature is enhanced. First-principles calculations are done to uncover the mechanism. The adsorption energy of NO_2 on the six-coordinated Ce of the CeO_2{100} polar plane is the most negative, indicating the most preferred sites for the adsorption of NO_2. However, if more O_v are generated, the proportion of six-coordinated Ce atoms will be reduced, and the interaction with NO_2 will be reduced because of charge recombination. Consequently, the sensing performances toward NO_2 are deteriorated. The results provide new information pertaining to the design and fabrication of room-temperature sensing materials for NO_2.

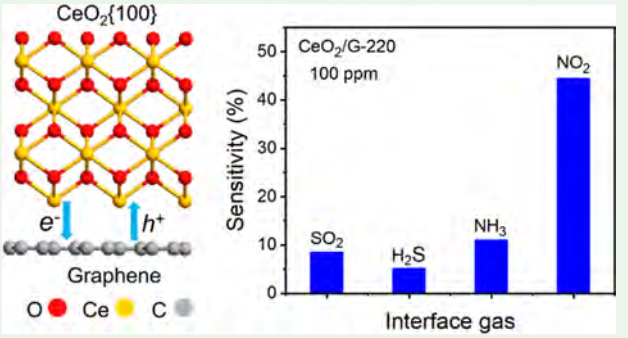

KEYWORDS: *polar CeO_2{100} plane, graphene, room-temperature gas sensing, charge recombination, oxygen vacancy, six-coordinated Ce atoms*

1. INTRODUCTION

Emission of toxic, harmful, and explosive gases poses serious threats to the modern society and NO_2 is one of the harmful atmospheric pollutants.[1−3] Long-term exposure to NO_2 albeit at the ppb level can be detrimental to the respiratory system and acid rain is another environmental concern.[1−3] Hence, timely and accurate detection of NO_2 is crucial. Because of its natural abundance and stability, CeO_2 is a common gas-sensing material.[4−7] *Barreca* et al. have prepared CeO_2 by chemical vapor deposition and demonstrated excellent NO_2-sensing response at 573.15 K.[7] *Hemalatha and Rukmani* have synthesized polyvinyl alcohol−CeO_2 nanocomposites with good NO_2 sensing properties at 423.15 K.[8] However, the high operating temperature, large energy consumption, safety hazards, and poor stability have limited wider applications,[4−8] and therefore, the development of advanced NO_2 sensors with high sensitivity, high selectivity, and rapid response and recovery for room temperature (RT) application is crucial.

The poor NO_2 sensing properties of metal oxides are mainly attributed to the low electrical conductivity at RT.[9−15] It has recently been observed that the electrical conductivity can be enhanced if the metal oxide is deposited on conductive materials such as carbonaceous materials.[9−15] For example, *Molina* et al. have found that NO_2 sensing at RT is better if the CeO_2 nanoparticles were anchored on carbon nanotubes. The response and recovery times for detection of 100 ppm NO_2 at RT were about 22.9 and 345.2 s, respectively.[9] *Oliva* et al. have fabricated NO_2 sensors with high sensitivity by depositing Yb-doped nickel oxide or hydroxide on carbon nanotubes and the response and recovery time for 100 ppm NO_2 at RT were about 16 and 252 s, respectively.[10] Compared with carbon nanotubes, graphene has a larger surface area, better carrier mobility, and more adsorption sites besides good electrical conductivity.[11−15] Composites comprising CeO_2 and graphene have been reported as NO_2 sensing materials at RT.[16−18] *Fu* et al. have prepared CeO_2/graphene composites showing rapid response to NO_2 at RT and excellent selectivity to NO_2 in the presence of O_2, CO, H_2, and NH_3.[16] The sensitivity of CeO_2/graphene composites for 100 ppm NO_2 gas increases by 4.6 times in comparison with the pure CeO_2 nanoparticles and the lowest detection limit is down to 5 ppm. When the concentration of NO_2 is increased from 5 ppm up to 300 ppm, the response time is shortened from 18.8 to 1.3 s, while the sensitivity increases from 3.78 to 12.76%.[16] *Su* et al. have observed that the RT sensitivity of CeO_2 nanoparticles/

Received: April 5, 2023
Accepted: May 30, 2023
Published: June 9, 2023

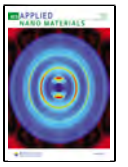

ACS Publications © 2023 American Chemical Society

https://doi.org/10.1021/acsanm.3c01513
ACS Appl. Nano Mater. 2023, 6, 10551−10558

graphene composites for NO_2 can be improved by ultraviolet light irradiation. The sensitivity enhancement is 51 times, and the lowest detection limit is 300 ppb, although ultraviolet light is harmful.[18]

The gas sensing response is related to the crystal plane of the metal oxide and a high-energy crystal plane with more low-coordinated atoms provides more active sites for better NO_2 sensing response.[19−22] *Wang* et al. have observed that the sensitivity of the {332} crystal plane of SnO_2 is better than that of the {111} crystal plane and the operating temperature and response time can be lowered.[20] *Xu* et al. have demonstrated that the high-energy {0001} facet of ZnO has better ethanol sensing response compared to the $\{01\bar{1}0\}$ facet and *Yang* et al. have illustrated that the high-energy {001} facet of TiO_2 exhibits enhanced sensing response toward acetone.[22] However, it is difficult to expose the high-energy crystal planes during growth, and furthermore, the sensing mechanism on high-energy crystal planes is still not well understood.[19−22]

Herein, composites of CeO_2 nanoparticles with high-energy {100} polar plane exposed and graphene are prepared hydrothermally. The proportion of Ce^{3+} and oxygen vacancy (O_v) is found to decrease with the increase in the hydrothermal temperature. Consequently, the RT NO_2 sensing response is enhanced considerably and the mechanism is discussed.

2. EXPERIMENTAL DETAILS

2.1. Preparation of CeO_2 and Graphene Composites. Graphene oxide was prepared by the modified hummers technique and then reduced with hydrazine hydrate at 353.15 K for 180 min.[23] Graphene (10 mg) was placed in a solution containing 20 mL of ethylene glycol and 20 mL of H_2O and after sonication for 120 min, 0.49 mmol $Ce(NO_3)_3{\cdot}6H_2O$, 1.48 mmol NaOH, and 300 mg of PVP were added, stirred magnetically for 3 h, transferred to a 100 mL autoclave with a poly(tetrafluoroethylene) lining, and heated to 433.15, 453.15, 463.15, 473.15, or 493.15 K for 24 h. After the reaction, the sediment was rinsed with ethanol and H_2O six times, collected by centrifugation, and dried at 323.15 K in vacuum for 10 h (Figure 1a). The samples were designated as CeO_2/G-a, CeO_2/G-b, CeO_2/G-c, CeO_2/G-d, and CeO_2/G-e according to the synthesis temperature.

2.2. Structural Characterization. X-ray diffraction (XRD) patterns (Bruker D8 ADVANCE, Cu K_α) and Raman scattering (wavelength of 633 nm) were performed to analyze the samples. Scanning electron microscopy (SEM) and transmission electron microscopy (TEM) were carried out on the Zeiss GeminiSEM 500 and JEOL-JEM-2100 Plus at 200 kV. The chemical states of the CeO_2/graphene composites were determined by X-ray photoelectron spectroscopy (XPS, Thermo Fisher ESCALAB Xi^+).

2.3. Fabrication and Assessment. 20 mg of the CeO_2/graphene composites were dispersed in 0.5 mL of deionized water and sonicated for 1.5 h. The dispersion (15 μL) was dropped onto the Au interdigital electrode 20 mm long, 10 mm wide, and 0.6 mm tall with a 100 μm channel width and left at RT for 12 h (Figure 1b). The sensing properties were determined on the CGS-4TPs system. The sensitivity (S_g) was determined by $S_g = \frac{R_a - R_g}{R_a}$, in which R_g and R_a represented the resistances in air and the target gas at RT, respectively. The response and recovery time corresponded to the time the total resistance was changed by 90% in the presence and absence of target gas.

2.4. Calculation Model and Method. The first-principles calculations were performed using the Vienna ab initio simulation package.[24−26] The Perdew−Burke−Ernzerhof functional was taken to describe the electronic exchange energy with an energy cutoff of 500 eV. The 3 × 3 × 1 matrix was chosen for the Monkhorst−Pack *k*-points, and 10^{-4} eV and 0.05 eV/Å were set as the energy and force convergences, respectively. The Bader charge analysis was done and the adsorption energy (E_a) of NO_2 on CeO_2 was defined as[27]

$$E_a = E_{CeO_2+NO_2} - E_{CeO_2} - E_{NO_2} \quad (1)$$

where $E_{CeO_2+NO_2}$, E_{CeO_2}, and E_{NO_2} are the energy of NO_2 adsorbed on CeO_2, isolated CeO_2, and NO_2 molecules, respectively. A more negative adsorption energy indicated stronger adsorption.[26]

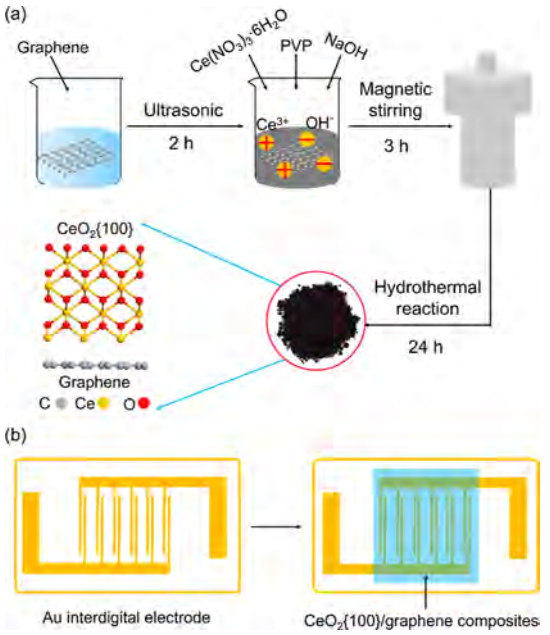

Figure 1. (a) Preparation of CeO_2{100}/graphene composites and (b) schematic of the gas sensor.

3. RESULTS AND DISCUSSION

3.1. Morphology and Structure. Figure 2 presents the XRD patterns of the CeO_2 and graphene composites. The 2θ peaks at 28.43, 33.03, 47.46, 56.29, 59.02, 69.47, 76.81, 79.18, and 88.51° can be indexed to the {111}, {200}, {220}, {311}, {222}, {400}, {331}, {420}, and {422} crystal planes of cubic CeO_2, respectively. The XRD peaks become stronger and sharper when the synthesis temperature is raised from 433.15 to 493.15 K. According to the Scherrer formula, the average grain sizes of CeO_2 of samples a−e are about 8.62, 10.13, 15.51, 20.27, and 31.18 nm, respectively. Figure 3 presents the Raman scattering spectra in which the peaks at about 1324 and

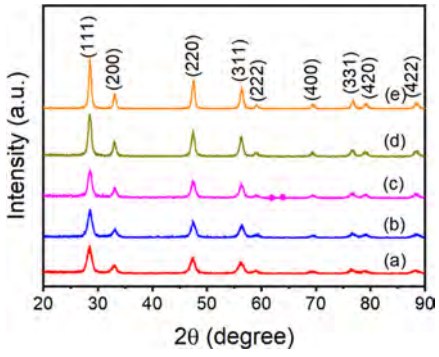

Figure 2. XRD patterns of the CeO_2/graphene composites prepared hydrothermally at different temperatures: (a) 433.15, (b) 453.15, (c) 463.15, (d) 473.15, and (e) 493.15 K.

https://doi.org/10.1021/acsanm.3c01513
ACS Appl. Nano Mater. 2023, 6, 10551−10558

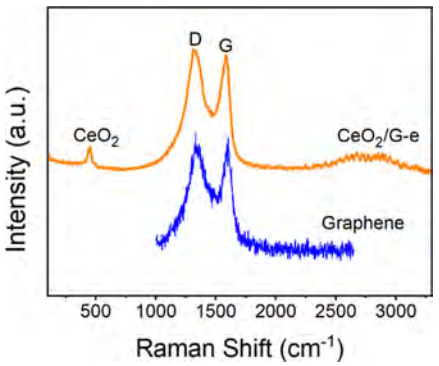

Figure 3. Raman scattering spectra of the graphene and CeO_2/graphene composites (CeO_2/G-e) prepared at 493.15 K.

1585 cm^{-1} are the D and G bands of graphene which is red-shifted slightly compared to pure graphene.[28,29] The Raman peak at 448 cm^{-1} is associated with the E_{2g} mode of CeO_2.[30] These results confirm the successful preparation of the CeO_2 and graphene composites.

The morphology of the CeO_2 and graphene composites is examined by FE-SEM. As shown in Figure S1(a1,a2), the CeO_2 nanoparticles are distributed evenly on graphene. Graphene usually contains oxygen functional groups and defects that promote nucleation and growth of CeO_2 nanoparticles. The size of the CeO_2 nanoparticles prepared at 433.15 K is about 8 nm [Figure S1(a3)]. If the temperature is increased to 453.15 K [Figure S1(b1−b3)], 463.15 K [Figure S1(c1−c3)], 473.15 K [Figure S1(d1−d3)], and 493.15 K [Figure S1(e1−e3)], the sizes of CeO_2 nanoparticles go up to 11, 15, 21, and 30 nm, respectively.

Figure 4 displays the TEM images. The irregular truncated cubic structure is observed if the hydrothermal process is performed at 433.15 K [Figure 4(a1,a2)]. The lattice spacing of 0.27 nm represents the {100} facet of CeO_2 and that of 0.32 nm at the cubic cutting corner represents the {111} facet of CeO_2 [Figure 4(a3)]. If the temperature is elevated further to 453.15 K [Figure 4(b1−b3)], 463.15 K [Figure 4(c1−c3)], 473.15 K [Figure 4(d1−d3)], and 493.15 K [Figure 4(e1−e3)], the cubic cutting corner disappears gradually, and the CeO_2 nanoparticles morph into regular cubes with the low-energy {111} facets disappearing gradually and the surface area of the high-energy {100} facets increasing (Figure S2). The SAED patterns of CeO_2/graphene composites prepared at 433.15 and 463.15 K are shown in Figure S3. The diffraction rings of CeO_2(111), (200), (220), and (222) planes were obviously observed providing evidence that the {100} facet is formed.

XPS is carried out to determine the chemical states. The peaks of Ce 4d, C 1s, O 1s, Ce $3d_5$, and Ce $3d_3$ were observed from the XPS survey spectra (Figure S4a). The high-resolution C 1s spectrum can be deconvoluted into three peaks, C−C at 284.8 eV, C−O (hydroxyl and epoxy) at 286.47 eV, as well as C═O (carboxyl) at 288.53 eV (Figure S4b). Figure S4c−f shows the Ce 3d spectra in which the peaks at 885.57 (V) and 903.9 eV (V*) are the $3d_{5/2}$ and $3d_{3/2}$ spin orbitals of Ce_2O_3 confirming the existence of Ce^{3+} and O_v.[31−35] Figure S5 shows the O 1s spectra. The deconvoluted high-resolution O 1s spectra show three peaks including lattice oxygen of CeO_2

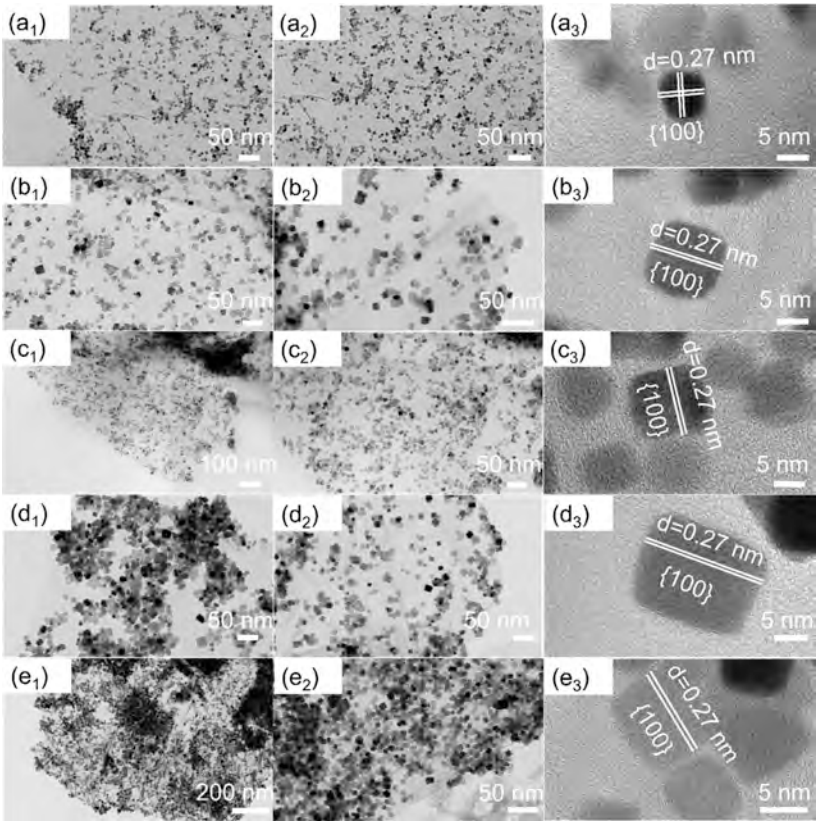

Figure 4. TEM and HR-TEM images of the CeO_2/graphene composites prepared at (a1−a3) 433.15, (b1−b3) 453.15, (c1−c3) 463.15, (d1−d3) 473.15, and (e1−e3) 493.15 K.

https://doi.org/10.1021/acsanm.3c01513
ACS Appl. Nano Mater. 2023, 6, 10551−10558

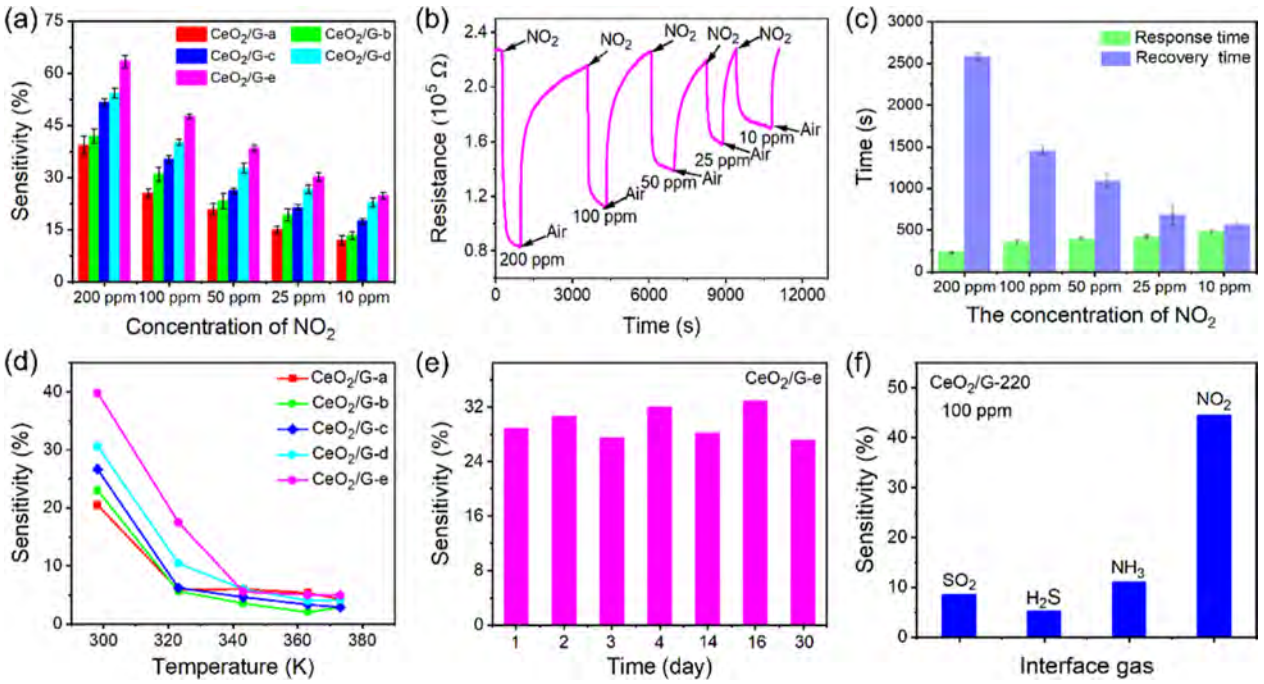

Figure 5. (a) Sensitivity of the CeO_2/graphene composites prepared at a different temperature for sensing of 200, 100, 50, 25, and 10 ppm NO_2 at RT; (b) real-time resistance curve of the CeO_2/G-e sensors as a function of NO_2 concentrations (10−200 ppm) at RT; (c) response and recovery time of the CeO_2/G-e sensors as a function of NO_2 concentrations (10−200 ppm) at RT; (d) sensitivity of the CeO_2/graphene composites for 5 ppm of NO_2 at 298.15, 323.15, 343.15, 363.15, and 373.15 K; (e) long-term stability of the CeO_2/G-e sensors at RT; and (f) sensitivity of the CeO_2/G-e sensors for different gases at RT.

(O_L) at 528.7 eV, adsorbed oxygen (O_{abs}) at 532.05 eV, and lattice oxygen of Ce_2O_3 (O*) at 533.23 eV.[31−35] As the synthesis temperature is increased from 433.15 to 493.15 K, the concentration of Ce^{3+} decreases from 25.46 to 16.6% and that of O* drops from 10.12 to 3%. The atomic ratios of C, Ce, and O determined by XPS are listed in Table S1. The atomic ratios of Ce and O in all the composites are not 1:2 due to oxygen vacancies. The Ce/O ratio is closer to 1:2 at the higher hydrothermal temperature showing that the concentration of O_v decreases with hydrothermal temperature going up.

3.2. Sensing Properties. The effects of different amounts of CeO_2/graphene composites on the NO_2 sensing response were studied, and the results are shown in Figure S6. The response for 10 ppm NO_2 is almost the same as the amount is increased from 20 to 50 g/L, while it deteriorates if the amount is higher. Hence, the 20 mg CeO_2/graphene composites are dispersed in 0.5 mL of deionized water to fabricate the sensors. Figure 5a shows the NO_2 sensing sensitivity of the CeO_2/graphene composites and CeO_2/G-e exhibits the highest sensitivity. The sensitivities for 200, 100, 50, 25, and 10 ppm NO_2 are 63.62, 48.10, 38.82, 30.85, and 24.94% corresponding to enhancements by 61.14, 88.54, 78.65, 97.12, and 101.1% referenced to CeO_2/G-a. As the temperature goes up, the corner defects in cubic CeO_2 disappear gradually, and the high-energy {100} facets become more abundant. Consequently, the sensing activity is enhanced. In addition, the NO_2-sensing response of CeO_2/graphene composites which were prepared at 523.15 and 543.15 K is studied, and the result is shown in Figure S7. The sensitivity is almost the same if the hydrothermal temperature is further increased up to 523.15 and 543.15 K. Figure 5b shows the real-time resistance of CeO_2/G-e for 200, 100, 50, 25, and 10 ppm of NO_2 at RT. The resistance declines sharply when exposed to NO_2 but recovers to the initial value after exposure to air. It is because NO_2 attracts electrons from CeO_2, and the electron density in the CeO_2/graphene composites decreases, while the hole density goes up.[36−40] Consequently, the electrical conductivity increases because the CeO_2/graphene composites is a p-type semiconductor. The response time increases from 250 s for 200 ppm to 618 s for 10 ppm, and the recovery time decreases from 2590 s for 200 ppm to 723 s for 10 ppm (Figure 5c).

The lowest detection limit (LOD) is calculated, and the results are shown in Figure S8 and Table S2. The LODs of CeO_2/G-a, CeO_2/G-b, CeO_2/G-c, CeO_2/G-d, and CeO_2/G-e sensor are 3.4, 3.02, 1.87, 1.51, and 1.5 ppm, respectively, suggesting that the RT NO_2 sensing response can be improved by increasing the percentage of high-energy {100} crystal plane. As shown in Figure 5d, the sensitivity for 50 ppm NO_2 decreases substantially with the increase in temperature. At RT, oxygen physisorbed on the surface of the sensor forms O_2^- and NO_2 reacts with O_2^- to improve the NO_2 sensing response.[36−40] At a higher operating temperature, the density of O_2^- decreases and O^- is formed. The NO_2 molecules are unable to react with O^- and the sensing response deteriorates.[36−40] In addition, at a higher temperature, desorption is accelerated. There is not enough long time for the sensors to react with NO_2 resulting in a poorer response.[36−40]

Figure 5e shows the long-term stability of CeO_2/G-e, and the sensitivity is maintained even after 30 days. Figure 5f displays the sensitivity of CeO_2/G-e toward other gases and the sensitivity toward NO_2 is much higher, indicating the good selectivity. The response is related to adsorbed oxygen. At RT, the adsorbed oxygen is O_2^- and NO_2 molecules react with O_2^- at RT, while the other gas molecules cannot react.[38,39] The adsorption energy of NO_2, NH_3, and SO_2 on the CeO_2{100}

https://doi.org/10.1021/acsanm.3c01513
ACS Appl. Nano Mater. 2023, 6, 10551−10558

facet is derived by first-principles calculation. As shown in Figure S9, the adsorption energy of NO_2 on the $CeO_2\{100\}$ facet is more negative than that of other gases, further demonstrating that the $CeO_2\{100\}$ facet facilitates the adsorption of NO_2. The effects of humidity on the NO_2 sensing performance of CeO_2/graphene composites are investigated, and the result is shown in Figure S10. The sensitivity decreases from 26.53 to 1.82% when the relative humidity changes from 33 to 82% at RT due to competitive adsorption between NO_2 and H_2O. In higher humidity, physisorbed water molecules occupy the adsorption sites and react with oxygen ions to form poor reactive hydroxyl groups (OH^-) and the active adsorption sites for NO_2 is decreased, resulting in poorer NO_2-sensing response.[40]

The performance of our sensor is compared to those of recently reported ones as shown in Table S3. Although the recovery time of SnO_2,[41] WO_3,[42] CeO_2,[43] and CeO_2/Al_2O_3[44] are 360, 560, 438, and 27 s, respectively, and less than that of the CeO_2/graphene composites, the operating temperature is higher (>100 °C). MoS_2 can be applied in RT NO_2 sensing, but the resistance recovers by only 50% at RT.[45,46] UV light irradiation can shorten the recovery time of MoS_2 at RT, but it causes health hazards. The operating temperatures of Cu/MoS_2,[47] MoS_2/graphene,[48] SnO_2/graphene,[12] WO_3/graphene,[13] NiO/graphene,[14] and SnO_2/graphene[15] are 100, 160, 50, 250, and 200 °C, respectively, and higher than that of the CeO_2/graphene composites in this work. Although the composites of graphene and CeO_2 nanoparticles with low-energy {111} facet exposed show fast response and recovery to NO_2 at RT, the sensitivity is lower than that of $CeO_2\{100\}$/graphene composites and UV light must be used to enhance the response at RT.[16,18] All in all, our sensor has better comprehensive sensing properties at RT without the need for thermal treatment or UV exposure.

3.3. Sensing Mechanism. In general, upon exposure to air, O_2 absorbs and captures electrons from the composites to produce O_2^- at RT. When the sensor is exposed to NO_2, NO_2 molecules react with adsorbed oxygen to capture electrons, and the hole density increases.[47−53] Since the electron affinity to NO_2 (2.27 eV) is higher than that to O_2 (0.45 eV),[47] the CeO_2/graphene composites behave as a p-type semiconductor with the decrease in resistance.[47−53]

$$O_{2(gas)} + e^- \rightarrow O^-_{2(ads)} \quad (2)$$

$$NO_{2(gas)} + O^-_{2(ads)} + 2e^- \rightarrow NO^-_{2(ads)} + 2O^-_{(ads)} \quad (3)$$

$$NO_{2(gas)} + O^-_{(ads)} \rightarrow NO^-_{3(ads)} \quad (4)$$

$$NO_{2(gas)} + e^- \rightarrow NO^-_{2(ads)} \quad (5)$$

Because the Fermi level of the $CeO_2\{100\}$ plane is higher than that of graphene,[53] electrons are transferred from CeO_2 to graphene, resulting in an electron depletion layer and negative charge region in CeO_2 and graphene, respectively (Figure 6a,b). A built-in electric field forms in equilibrium. Upon exposure to NO_2, NO_2 captures electrons from the CeO_2 nanoparticles, and the built-in electric field is broken, so that extra holes diffuse into graphene until a new balance is reached.[48−53] Therefore, the resistance of the CeO_2/graphene composites decreases.

The graphene plays an important role in enhancing the NO_2 response. First, the oxygen-containing functional groups on graphene have negative charges so that positively charged Ce^{3+}

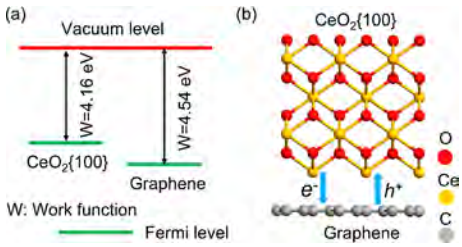

Figure 6. (a) Work functions of $CeO_2\{100\}$ facet and graphene and (b) schematic showing the sensing mechanisms of $CeO_2\{100\}$/graphene composites for NO_2.

adsorbs onto graphene and is oxidized to suppress agglomeration and recrystallization of CeO_2 nanoparticles.[15−18] Second, graphene as a conductive network improves the electrical conductivity of CeO_2 nanoparticles.[15] Third, the large specific surface area of graphene benefits the adsorption of NO_2, and fourth, the heterojunction formed between CeO_2 and graphene inhibits the recombination of electrons and holes to enhance the NO_2 response.[15−18]

The mechanism of the enhancement rendered by the high-energy {100} facet is studied. Structurally, the $CeO_2\{111\}$ plane is stacked with the repeating O−Ce−O sandwiched structure, in which each Ce atom is bonded with seven O atoms with one dangling bond and each O atom is bonded with three Ce atoms with one dangling bond. The $CeO_2\{100\}$ plane is composed of alternating O and Ce layers, in which each Ce atom is bonded with six O atoms with two dangling bonds, and each O atom is bonded with two Ce atoms with two dangling bonds.[54] Hence, there are more dangling bonds on the {100} facets than the {111} facets. The composites of graphene and CeO_2 nanoparticles with more exposed {100} facets have better NO_2 response at RT. In addition, Ce atoms are positively charged, but O atoms are negatively charged on the $CeO_2\{100\}$ facet (Figure 7a) and therefore, the positive

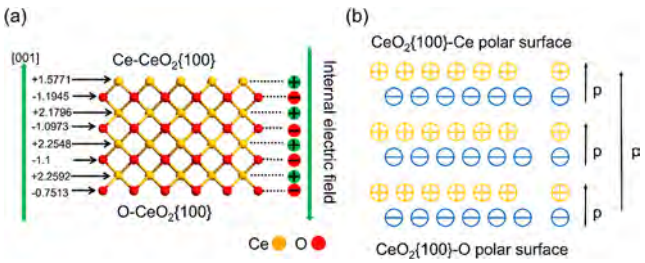

Figure 7. (a) Atomic charge distribution and (b) space charge distribution of the $CeO_2\{100\}$ polar plane.

and negative charge centers do not coincide and polarization occurs spontaneously on the $CeO_2\{100\}$ facet (Figure 7b).[51,52] Since NO_2 is a polar molecule, an electrostatic force is induced when NO_2 adsorbs on the $CeO_2\{100\}$ facet to boost the interactions between NO_2 and the {100} polar plane. Generally, a higher concentration of O_v gives rise to better NO_2 response. However, the response at RT decreases with the increase in proportion of Ce^{3+} and O_v. To understand this inconsistency, the adsorption energy (E_a) of NO_2 on the $CeO_2\{100\}$ facet is calculated. As shown in Figure S11a, the E_a value of NO_2 on Ce atoms is bigger than that of NO_2 on O_v. Hence, the six-coordinated Ce atoms on the {100} polar plane constitute the optimal adsorption sites for NO_2 (Figure S11b). If O_v exists on the $CeO_2\{100\}$ polar plane, two Ce^{4+} ions are

https://doi.org/10.1021/acsanm.3c01513
ACS Appl. Nano Mater. 2023, 6, 10551−10558

converted into Ce^{3+} to achieve charge neutrality ($2Ce^{4+} + O^{2-} \rightarrow 2Ce^{3+} + O_v + 0.5O_2$).[4] When the hydrothermal temperature is elevated, the concentrations of O_v and Ce^{3+} decrease and the six-coordinated Ce atoms increase. Consequently, the polarity and interactions between NO_2 and the {100} facet is enhanced, showing the better NO_2-sensing response.[55]

4. CONCLUSIONS

Composites of cubic CeO_2 nanoparticles with the exposed {100} facet and graphene are prepared hydrothermally. As the hydrothermal temperature goes up, the percentage of the high-energy {100} polar plane of CeO_2 increases, but those of Ce^{3+} and O_v decrease. Consequently, the six-coordination Ce atoms on the polar plane increase. First-principles calculation reveals that the adsorption energy of NO_2 on the six-coordination Ce atoms is more negative, and hence, adsorption of NO_2 is more favorable on the {100} polar plane of CeO_2. Moreover, when the proportion of O_v is reduced, the polarity of the CeO_2{100} facet improves, and the interactions between NO_2 and the {100} facet are enhanced. As a result, the NO_2 sensing response on the CeO_2{100} facet is improved at RT. The results provide insights into the design and fabrication of high-performance sensing materials for NO_2 at RT.

■ ASSOCIATED CONTENT

Supporting Information

The Supporting Information is available free of charge at https://pubs.acs.org/doi/10.1021/acsanm.3c01513.

SEM images of CeO_2/graphene composites; schematic illustrations of the CeO_2{100} polar plane with the increase in hydrothermal temperature; SAED patterns of CeO_2/graphene composites; XPS and gas-sensing performance of CeO_2/graphene composites; and adsorption energy of NO_2 on the CeO_2{100} crystal plane (PDF)

■ AUTHOR INFORMATION

Corresponding Authors

Taotao Ai − *School of Materials Science and Engineering, Shaanxi University of Technology, Hanzhong 723001 Shaanxi, China*; Email: aitaotao0116@126.com

Fei Ma − *State Key Laboratory for Mechanical Behavior of Materials, Xi'an Jiaotong University, Xi'an 710049 Shaanxi, China*; orcid.org/0000-0002-3911-7121; Email: mafei@mail.xjtu.edu.cn

Paul K. Chu − *Department of Physics, Department of Materials Science and Engineering, and Department of Biomedical Engineering, City University of Hong Kong, Kowloon 999077 Hong Kong, China*; orcid.org/0000-0002-5581-4883; Email: paul.chu@cityu.edu.hk

Authors

Lizhai Zhang − *School of Materials Science and Engineering, Shaanxi University of Technology, Hanzhong 723001 Shaanxi, China; State Key Laboratory for Mechanical Behavior of Materials, Xi'an Jiaotong University, Xi'an 710049 Shaanxi, China; Department of Physics, Department of Materials Science and Engineering, and Department of Biomedical Engineering, City University of Hong Kong, Kowloon 999077 Hong Kong, China*; orcid.org/0000-0002-6474-9518

Huiyan Xu − *Institute for Smart Materials and Engineering, University of Jinan, Jinan 250022 Shandong, China*; orcid.org/0000-0001-7269-9269

Yuhong Huang − *College of Physics and Information Technology, Shaanxi Normal University, Xi'an 710062 Shaanxi, China*

Hongbing Lu − *College of Physics and Information Technology, Shaanxi Normal University, Xi'an 710062 Shaanxi, China*; orcid.org/0000-0001-5910-2106

Kewei Xu − *Department of Physics and Opt-Electronic Engineering, Xi'an University of Arts and Science, Xi'an 710065 Shaanxi, China*

Complete contact information is available at: https://pubs.acs.org/10.1021/acsanm.3c01513

Author Contributions

The manuscript was written based on contributions from all the authors. All the authors approved the manuscript.

Notes

The authors declare no competing financial interest.

■ ACKNOWLEDGMENTS

This work was jointly supported by National Natural Science Foundation of China (grant no. 51771144), Natural Science Foundation of Shaanxi Province (nos. 2021JC-06, 2019TD-020, and 2023-JC-QN-0476), Shaanxi University of Technology Research Grant (no. SLGRCQD2207), City University of Hong Kong Donation Research Grant (DON-RMG no. 9229021), City University of Hong Kong Strategic Research Grant (SRG no. 7005505), and City University of Hong Kong Donation Grant (no. 9220061).

■ REFERENCES

(1) Hu, W.; Wan, L. T.; Jian, Y.; Ren, C.; Jin, K.; Su, X. H.; Bai, X.; Haick, H.; Yao, M. S.; Wu, W. Electronic noses: from advanced materials to sensors aided with data processing. *Adv. Mater. Technol.* **2018**, *4*, 1800488.

(2) Dung, T. T.; Oh, Y.; Choi, S. J.; Kim, I. D.; Oh, M. K.; Kim, M. Applications and advances in bioelectronic noses for odour sensing. *Sensors* **2018**, *18*, 103.

(3) Lee, S. W.; Lee, W.; Hong, Y.; Lee, G.; Yoon, D. S. Recent advances in carbon material based NO_2 gas sensors. *Sens. Actuators, B* **2018**, *255*, 1788−1804.

(4) Wang, Z. M.; Yu, R. B. Hollow micro/nanostructured ceria-based materials: Synthetic strategies and versatile applications. *Adv. Mater.* **2019**, *31*, 1800592.

(5) Michel, C. R.; Martínez-Preciado, A. H. CO sensor based on thick films of 3D hierarchical CeO_2 architectures. *Sens. Actuators, B* **2014**, *197*, 177−184.

(6) Izu, N.; Shin, W.; Matsubara, I.; Murayama, N. Influence of SO_2 gas on output of resistive oxygen sensors using CeO_2 and $Ce_{0.8}Zr_{0.2}O_2$. *J. Electrochem. Soc.* **2005**, *152*, H111.

(7) Barreca, D.; Comini, E.; Gasparotto, A.; Maccato, C.; Maragno, C.; Sberveglieri, G.; Tondello, E. Gas sensing properties of columnar CeO_2 nanostructures prepared by chemical vapor deposition. *J. Nanosci. Nanotechnol.* **2008**, *8*, 1012−1016.

(8) Hemalatha, K. S.; Rukmani, K. Poly vinyl alcohol-CeO_2 nanocomposite films: A promising material for NO_2 sensors at high temperatures. *Mater. Res. Express* **2019**, *6*, 085008.

(9) Molina, A.; Al-Sardar, M.; Rodriguez-Gonzalez, V.; Escobar-Barrios, V.; Zakhidov, A. A.; Mtz-Enriquez, A. I.; Encinas, A.; Oliva, J. Efficient NO_2 detection and the sensing mechanism of stretchable/biodegradable MWCNT based sensors decorated with CeO_2 nanoparticles. *Synth. Met.* **2022**, *287*, 117091.

(10) Molina, A.; Oliva, A. I.; Zakhidov, A.; Valadez-Renteria, E.; Rodriguez-Gonzalez, V.; Encinas, A.; Oliva, J. A highly sensitive and biodegradable NO_2 sensor made with CNTs and $Ni(OH)_2$/NiO:Yb microparticles. *J. Alloys Compd.* **2022**, *903*, 163896.
(11) Lim, N.; Kim, H.; Pak, Y.; Byun, Y. T. Enhanced NO_2 sensing performance of graphene with thermally induced defects. *Materials* **2021**, *14*, 2347.
(12) Zhang, H.; Feng, J. C.; Fei, T.; Liu, S.; Zhang, T. SnO_2 nanoparticles-reduced graphene oxide nanocomposites for NO_2 sensing at low operating temperature. *Sens. Actuators, B* **2014**, *190*, 472−478.
(13) Srivastava, S.; Jain, K.; Singh, V. N.; Singh, S.; Vijayan, N.; Dilawar, N.; Gupta, G.; Senguttuvan, T. D. Faster response of NO_2 sensing in graphene-WO_3 nanocomposites. *Nanotechnology* **2012**, *23*, 205501.
(14) Hoa, L. T.; Tien, H. N.; Luan, V. H.; Chung, J. S.; Hur, S. H. Fabrication of a novel 2D-graphene/2D-NiO nanosheet-based hybrid nanostructure and its use in highly sensitive NO_2 sensors. *Sens. Actuators, B* **2013**, *185*, 701−705.
(15) Li, L.; He, S. J.; Liu, M. M.; Zhang, C. M.; Chen, W. Three-dimensional mesoporous graphene aerogel-supported SnO_2 nanocrystals for high-performance NO_2 gas sensing at low temperature. *Anal. Chem.* **2015**, *87*, 1638−1645.
(16) Yang, Y.; Tian, C. G.; Sun, L.; Lu, R. J.; Zhou, W.; Shi, K. Y.; Kan, K.; Wang, J. C.; Fu, H. G. Growth of small sized CeO_2 particles in the interlayers of expanded graphite for high-performance room temperature NO_x gas sensors. *J. Mater. Chem. A* **2013**, *1*, 12742−12749.
(17) Jiang, X. X.; Tai, H. L.; Ye, Z. B.; Yuan, Z.; Liu, C. H.; Su, Y. J.; Jiang, Y. D. Novel P-N heterojunction-type RGO/CeO_2 bilayer membrane for room-temperature nitrogen dioxide detection. *Mater. Lett.* **2017**, *186*, 49−52.
(18) Hu, J.; Zou, C.; Su, Y. J.; Li, M.; Ye, X. Z.; Cai, B. F.; Kong, E. S. W.; Yang, Z.; Zhang, Y. F. Light-assisted recovery for a highly-sensitive NO_2 sensor based on RGO-CeO_2 hybrids. *Sens. Actuators, B* **2018**, *270*, 119−129.
(19) Han, X. G.; Jin, M. S.; Xie, S. F.; Kuang, Q.; Jiang, Z. Y.; Jiang, Y. Q.; Xie, Z. X.; Zheng, L. S. Synthesis of tin dioxide octahedral nanoparticles with exposed high-energy {221} facets and enhanced gas-sensing properties. *Angew. Chem.* **2009**, *121*, 9344−9347.
(20) Wang, C. X.; Cai, D. P.; Liu, B.; Li, H.; Wang, D. D.; Liu, Y.; Wang, L. L.; Wang, Y. R.; Li, Q. H.; Wang, T. H. Ethanol-sensing performance of tin dioxide octahedral nanocrystals with exposed high energy {111} and {332} facets. *J. Mater. Chem. A* **2014**, *2*, 10623−10628.
(21) Xu, J. Q.; Xue, Z. G.; Qin, N.; Cheng, Z. X.; Xiang, Q. The crystal facet-dependent gas sensing properties of ZnO nanosheets: Experimental and computational study. *Sens. Actuators, B* **2017**, *242*, 148−157.
(22) Yang, Y.; Hong, A. J.; Liang, Y.; Xu, K.; Yu, T.; Shi, J.; Zeng, F. Y.; Qu, Y. H.; Liu, Y. T.; Ding, M. Q.; Zhang, W.; Yuan, C. L. High-energy {001} crystal facets and surface fluorination engineered gas sensing properties of anatase titania nanocrystals. *Appl. Surf. Sci.* **2017**, *423*, 602−610.
(23) Marcano, D. C.; Kosynkin, D. V.; Berlin, J. M.; Sinitskii, A.; Sun, Z.; Slesarev, A.; Alemany, L. B.; Lu, W.; Tour, J. M. Improved synthesis of graphene oxide. *ACS Nano* **2010**, *4*, 4806−4814.
(24) Kresse, G.; Furthmüller, J. Efficient iterative schemes for ab initio total-energy calculations using a plane-wave basis set. *Phys. Rev. B: Condens. Matter Mater. Phys.* **1996**, *54*, 11169−11186.
(25) Kresse, G.; Hafner, J. Ab initio molecular dynamics for open-shell transition metals. *Phys. Rev. B: Condens. Matter Mater. Phys.* **1993**, *48*, 13115−13118.
(26) Kresse, G.; Joubert, D. From ultrasoft pseudopotentials to the projector augmented-wave method. *Phys. Rev. B: Condens. Matter Mater. Phys.* **1999**, *59*, 1758−1775.
(27) Xie, T.; Wang, X. D.; Yao, M.; Liu, X. S.; Chen, Y. G. First-principle study of CO adsorption and oxidation on Sm-doped CeO_2(111) surface. *RSC Adv.* **2016**, *6*, 20349−20356.
(28) Krishnamoorthy, K.; Veerapandian, M.; Mohan, R.; Kim, S. J. Investigation of raman and photoluminescence studies of reduced graphene oxide sheets. *Appl. Phys. A* **2012**, *106*, 501−506.
(29) Yang, D. X.; Velamakanni, A.; Bozoklu, G.; Park, S.; Stoller, M.; Piner, R. D.; Stankovich, S.; Jung, I.; Field, D. A.; Ventrice, C. A.; Ruoff, R. S. Chemical analysis of graphene oxide films after heat and chemical treatments by X-ray photoelectron and micro-raman spectroscopy. *Carbon* **2009**, *47*, 145−152.
(30) Kosacki, I.; Suzuki, T.; Anderson, H. U.; Colomban, P. Raman scattering and lattice defects in nanocrystalline CeO_2 thin films. *Solid State Ionics* **2002**, *149*, 99−105.
(31) Srivastava, M.; Das, A. K.; Khanra, P.; Uddin, M. E.; Kim, N. H.; Lee, J. H. Characterizations of in situ grown ceria nanoparticles on reduced graphene oxide as a catalyst for the electro-oxidation of hydrazine. *J. Mater. Chem. A* **2013**, *1*, 9792−9801.
(32) Dutta, D.; Chandra, S.; Swain, A. K. D.; Bahadur, D. Bahadur SnO_2 quantum dots-reduced graphene oxide composite for enzyme-free ultrasensitive electrochemical detection of urea. *Anal. Chem.* **2014**, *86*, 5914−5921.
(33) Wang, Z. L.; Yan, J. M.; Zhang, Y. F.; Ping, Y.; Wang, H. L.; Jiang, Q. Facile synthesis of nitrogen-doped graphene supported AuPd−CeO_2 nanocomposites with high-performance for hydrogen generation from formic acid at room temperature. *Nanoscale* **2014**, *6*, 3073−3077.
(34) Fang, S.; Xin, Y.; Ge, L.; Han, C.; Qiu, P.; Wu, L. Facile synthesis of CeO_2 hollow structures with controllable morphology by template-engaged etching of Cu_2O and their visible light photocatalytic performance. *Appl. Catal., B* **2015**, *179*, 458−467.
(35) Vinodkumar, T.; Naga Durgasri, D.; Reddy, B. M.; Alxneit, I. Synthesis and structural characterization of Eu_2O_3 doped CeO_2: Influence of oxygen defects on CO oxidation. *Catal. Lett.* **2014**, *144*, 2033−2042.
(36) Long, H.; Harley-Trochimczyk, A.; Pham, T.; Tang, Z.; Shi, T. L.; Zettl, A.; Carraro, C.; Worsley, M. A.; Maboudian, R. High surface area MoS_2/graphene hybrid aerogel for ultrasensitive NO_2 detection. *Adv. Funct. Mater.* **2016**, *26*, 5158−5165.
(37) Kwon, Y. J.; Kang, S. Y.; Wu, P.; Peng, Y.; Kim, S. S.; Kim, H. W. Selective improvement of NO_2 gas sensing behaviour in SnO_2 nanowires by ion-beam irradiation. *ACS Appl. Mater. Interfaces* **2016**, *8*, 13646−13658.
(38) Wu, E. X.; Xie, Y.; Yuan, B.; Zhang, H.; Hu, X. D.; Liu, J.; Zhang, D. H. Ultrasensitive and fully reversible NO_2 gas sensing based on p-type $MoTe_2$ under ultraviolet illumination. *ACS Sens.* **2018**, *3*, 1719−1726.
(39) Wang, Z.; Sackmann, A.; Gao, S.; Weimar, U.; Lu, G.; Liu, S.; Zhang, T.; Barsan, N. Study on highly selective sensing behaviour of ppb-level oxidizing gas sensors based on Zn_2SnO_4 nanoparticles immobilized on reduced graphene oxide under humidity conditions. *Sens. Actuators, B* **2019**, *285*, 590−600.
(40) Yoon, J. W.; Kim, J. S.; Kim, T. H.; Hong, Y. J.; Kang, Y. C.; Lee, J. H. A new strategy for humidity independent oxide chemiresistors: Dynamic self-refreshing of In_2O_3 sensing surface assisted by layer-by-layer coated CeO_2 nanoclusters. *Small* **2016**, *12*, 4229−4240.
(41) Comini, E.; Faglia, G.; Sberveglieri, G.; Pan, Z.; Wang, Z. L. Stable and highly sensitive gas sensors based on semiconducting oxide nanobelts. *Appl. Phys. Lett.* **2002**, *81*, 1869−1871.
(42) Urasinska-Wojcik, B.; Vincent, T. A.; Chowdhury, M. F.; Gardner, J. W. Ultrasensitive WO_3 gas sensors for NO_2 detection in air and low oxygen environment. *Sens. Actuators, B* **2017**, *239*, 1051−1059.
(43) Oosthuizen, D. N.; Motaung, D. E.; Swart, H. C. Gas sensors based on CeO_2 nanoparticles prepared by chemical precipitation method and their temperature-dependent selectivity towards H_2S and NO_2 gases. *Appl. Surf. Sci.* **2020**, *505*, 144356.
(44) Naik, M. C.; Bamane, S. R.; Pakhare, K. S.; Potdar, S. S.; Patil, U. M. Synthesis of CeO_2-Al_2O_3 nanocomposite by chemical combustion method for NO_2 gas−sensing application. *J. Mater. Sci.: Mater. Electron.* **2021**, *32*, 19925−19937.

https://doi.org/10.1021/acsanm.3c01513
ACS Appl. Nano Mater. 2023, 6, 10551−10558

(45) Kumar, R.; Goel, N.; Kumar, M. High performance NO_2 sensor using MoS_2 nanowires network. *Appl. Phys. Lett.* **2018**, *112*, 053502.
(46) Kumar, R.; Goel, N.; Kumar, M. UV activated MoS_2 based fast and reversible NO_2 sensor at room temperature. *ACS Sens.* **2017**, *2*, 1744−1752.
(47) Tyagi, S.; Kumar, A.; Kumar, A.; Gautam, Y. K.; Kumar, V.; Kumar, Y.; Singh, B. P. Enhancement in the sensitivity and selectivity of Cu functionalized MoS_2 nanoworm thin films for nitrogen dioxide gas sensor. *Mater. Res. Bull.* **2022**, *150*, 111784.
(48) Wang, Z.; Zhang, T.; Zhao, C.; Han, T.; Fei, T.; Liu, S.; Lu, G. Rational synthesis of molybdenum disulfide nanoparticles decorated reduced graphene oxide hybrids and their application for high-performance NO_2 sensing. *Sens. Actuators, B* **2018**, *260*, 508−518.
(49) Han, J. Y.; Kong, D. H.; Zhou, W. R.; Gao, Y. B.; Gao, Y.; Liu, G. N.; Liu, F. M.; Wang, C. G.; Sun, P.; Lu, G. Y. Variable dimensional structure and interface design of In_2O_3/rGO nanocomposites with oxygen vacancy for enhancing NO_2 sensing performance. *Sens. Actuators, B* **2022**, *371*, 132596.
(50) Wu, J.; Wu, Z. X.; Ding, H. J.; Wei, Y. M.; Huang, W. X.; Yang, X.; Li, Z. Y.; Qiu, L.; Wang, X. T. Three-dimensional graphene hydrogel decorated with SnO_2 for high-performance NO_2 sensing with enhanced immunity to humidity. *ACS Appl. Mater. Interfaces* **2020**, *12*, 2634−2643.
(51) Liu, S. W.; Wang, M. Y.; Ge, C. X.; Lei, S. Y.; Hussain, S.; Wang, M. S.; Qiao, G. J.; Liu, G. W. Enhanced room-temperature NO_2 sensing performance of SnO_2/Ti_3C_2 composite with double heterojunctions by controlling co-exposed {221} and {110} facets of SnO_2. *Sens. Actuators, B* **2022**, *365*, 131919.
(52) Han, Y. T.; Huang, D.; Ma, Y. J.; He, G. L.; Hu, J.; Zhang, J.; Hu, N. T.; Su, Y. J.; Zhou, Z. H.; Zhang, Y. F.; Yang, Z. Design of hetero-nanostructures on MoS_2 nanosheets to boost NO_2 room-temperature sensing. *ACS Appl. Mater. Interfaces* **2018**, *10*, 22640−22649.
(53) Zhang, L. Z.; Fang, Q. L.; Huang, Y. H.; Xu, K. W.; Ma, F.; Chu, P. K. Facet-engineered CeO_2/graphene composites for enhanced NO_2 gas-sensing. *J. Mater. Chem. A* **2017**, *5*, 6973−6981.
(54) Huang, W. X.; Gao, Y. X. Morphology-dependent surface chemistry and catalysis of CeO_2 nanocrystals. *Catal. Sci. Technol.* **2014**, *4*, 3772−3784.
(55) Capdevila-Cortada, M.; López, N. Entropic contributions enhance polarity compensation for CeO_2 (100) surfaces. *Nat. Mater.* **2016**, *16*, 328−334.

https://doi.org/10.1021/acsanm.3c01513
ACS Appl. Nano Mater. 2023, 6, 10551−10558

Supporting information

Polar Cubic CeO_2 Nanoparticles on Graphene for Enhanced Room-Temperature NO_2 Sensing Performance

Lizhai Zhang[a,b,c], Huiyan Xu[d], Yuhong Huang[e], Hongbing Lu[e], Taotao Ai[a], Kewei Xu[f], Fei Ma[b*], Paul k Chu[c*]*

[a] School of Materials Science and Engineering, Shaanxi University of Technology, Hanzhong 723001, Shaanxi, China

[b] State Key Laboratory for Mechanical Behavior of Materials, Xi'an Jiaotong University, Xi'an 710049, Shaanxi, China

[c] Department of Physics, Department of Materials Science and Engineering, and Department of Biomedical Engineering, City University of Hong Kong, Tat Chee Avenue, Kowloon, Hong Kong, China

[d] Institute for smart materials and engineering, University of Jinan, Jinan 250022, Shandong, China

[e] College of Physics and Information Technology, Shaanxi Normal University, Xi'an 710062, Shaanxi, China

[f] Department of Physics and Opt-electronic Engineering, Xi'an University of Arts and Science, Xi'an 710065, Shaanxi, China

*Address correspondence to: mafei@mail.xjtu.edu.cn (F. Ma), paul.chu@cityu.edu.hk (P. K. Chu), aitaotao0116@126.com (T. T. Ai).

The process of calculation of noise level (RMS_{Noise}) and limit of detection (LOD):[S1]

(1) Execute linear fit for the response curve versus NO_2 concentration of the sensor and then extract the slope value (sensitivity) and standard error in the linear regime, as shown in **Figure S8**.

(2) Take N = 50 data points at the baseline before NO_2 exposure and then plot the data (ΔR/R (%) versus Time (sec)) and then execute Polynomial fit (5th order) .

(3) Take regular residual of polynomial fit and calculate the root-mean squared deviation (***RMS_{Noise}***) and LOD with Equation 1 and 2.

$$RMS_{Noise}\left(ppm^{-1}\right) = \sqrt{V_x^2 / N} \quad \text{where} \quad V_x^2 = \sum \left(Y_i - \bar{Y}\right)^2 \tag{1}$$

$$Limit\ of\ \text{detection}\left(ppm\right) = 3 \times \frac{RMS_{Noise}}{Slope} \tag{2}$$

[S1] Duy, L. T.; Kim, D. J.; Trung, T. Q.; Dang, V. Q.; Kim, B. Y.; Moon, H. K.; Lee, N. E. High Performance Three-Dimensional Chemical Sensor Platform Using Reduced Graphene Oxide Formed on High Aspect-Ratio Micro-Pillars. *Adv. Funct. Mater.* **2015**, *25*, 883–890.

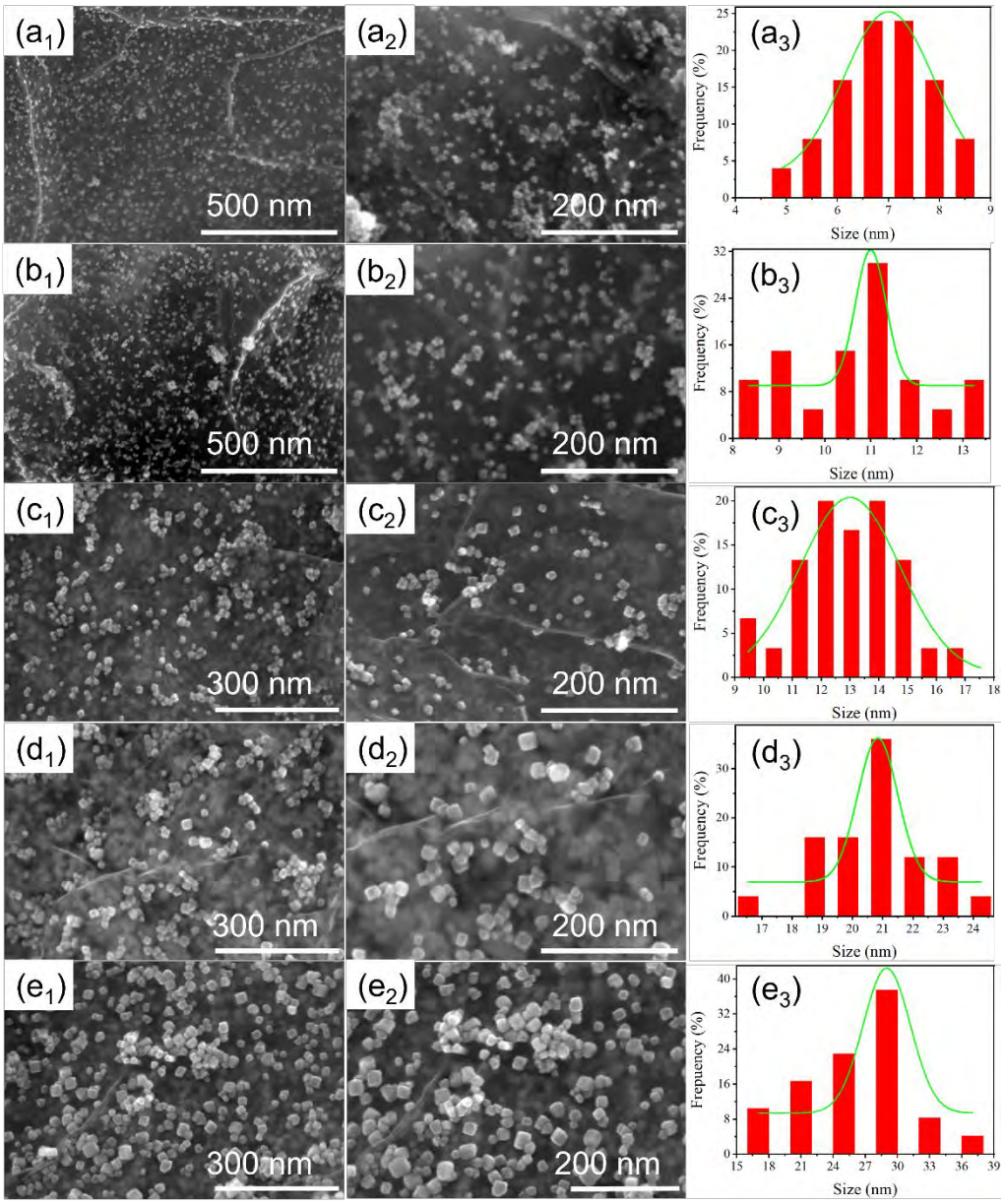

Figure S1. SEM images and grain size distributions of the CeO_2/graphene composites prepared at (a_1-a_3) 433.15 K, (b_1-b_3) 453.15 K, (c_1-c_3) 463.15 K, (d_1-d_3) 473.15 K, and (e_1-e_3) 493.15 K.

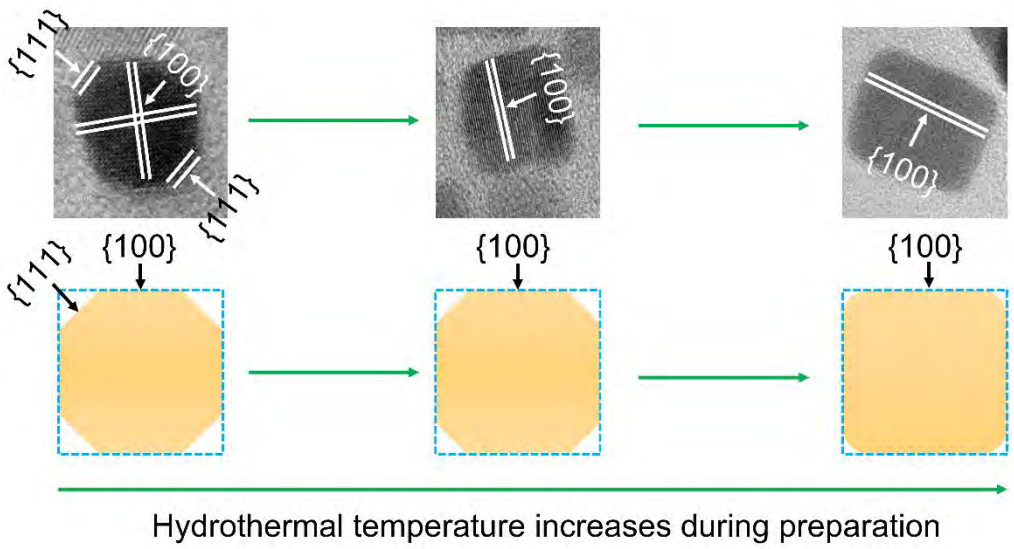

Figure S2. Schematic illustrations of the CeO_2{100} polar plane with increasing hydrothermal temperature

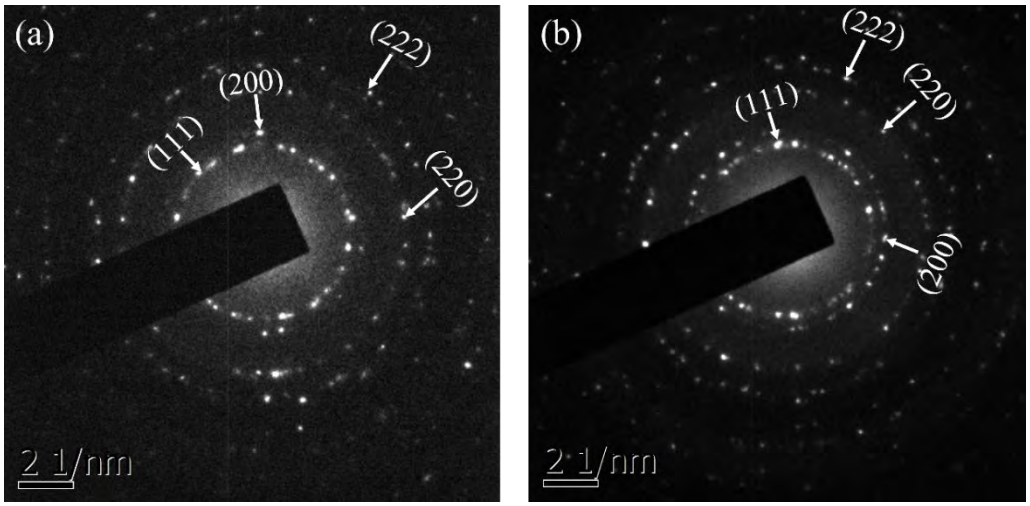

Figure S3. The SAED patterns of CeO_2/graphene composites prepared at (a) 433.15 K and (b) 463.15 K, respectivity.

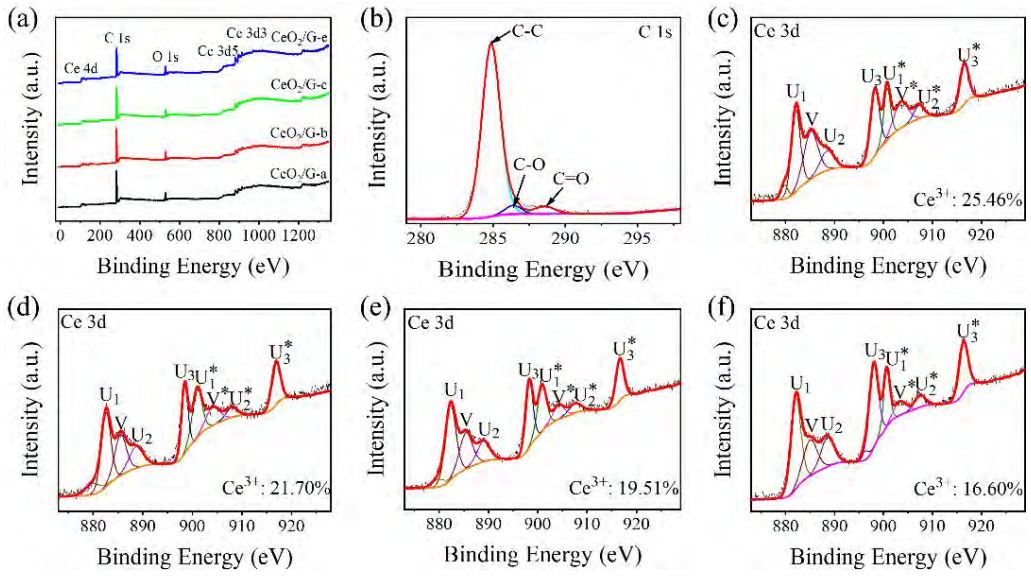

Figure S4. (a) XPS survey spectra of the CeO_2/graphene composites prepared hydrothermally at a different temperature; (b) C 1*s* XPS spectra of the CeO_2/G-e samples; Ce 3*d* XPS spectra of the CeO_2/graphene composites prepared at a different temperature: (c) 433.15 K, (d) 453.15 K, (e) 463.15 K, and (f) 493.15 K.

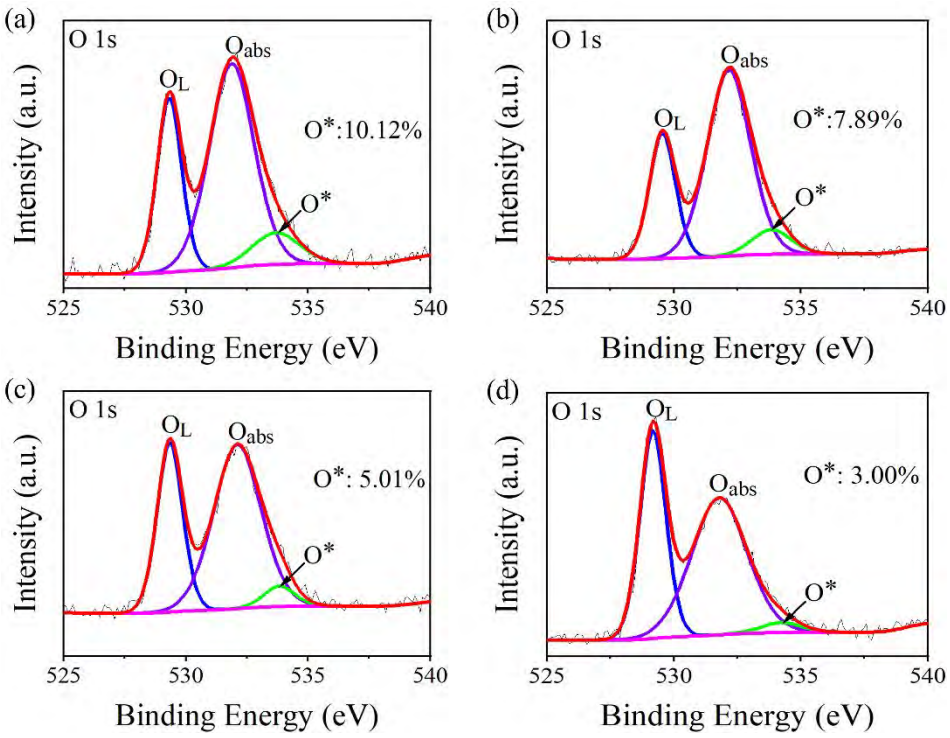

Figure S5. O 1*s* XPS spectra of the CeO_2/graphene composites prepared hydrothermally at a different temperature: (a) 433.15 K, (b) 453.15 K, (c) 463.15 K and (d) 493.15 K.

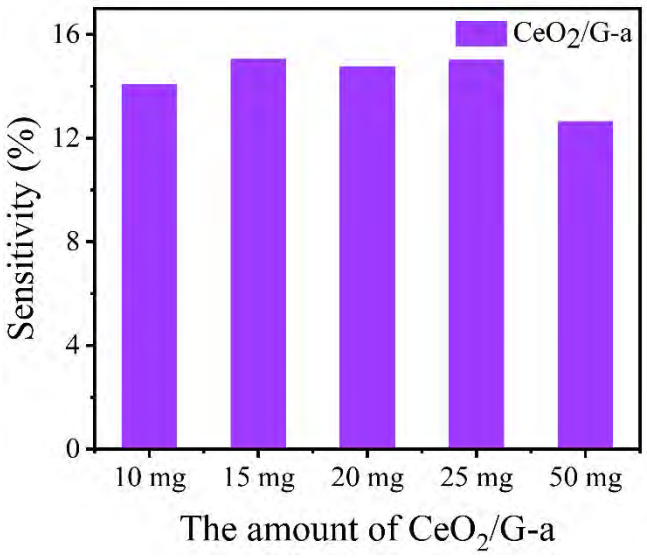

Figure S6. The sensitivity of the sensor toward 10 ppm NO_2 at RT with increasing the amount of CeO_2/graphene composites from 10 mg to 50 mg.

To study the role of amount of CeO_2/graphene composites on NO_2 sensing response, the 10 mg (20 g/L), 15 mg (30 g/L), 20 mg (40 g/L), 25 mg (50 g/L) and 50 mg (100 g/L) of CeO_2/graphene composites were dispersed into 0.5 mL of deionized water, respectively and the homogeneous solution was formed by sonicated for 1.5 h. 15 uL dispersion was dropped onto the Au interdigital electrode with 20 mm length, 10 mm width, 0.6 mm height as well as 100 μm channel width, and heated at RT for 12 h. The area of prepared samples onto the Au interdigital electrode was about 96 mm^2. In this paper, the thickness of prepared samples onto the Au interdigital electrode was controlled by changing the amount of CeO_2/graphene composites.

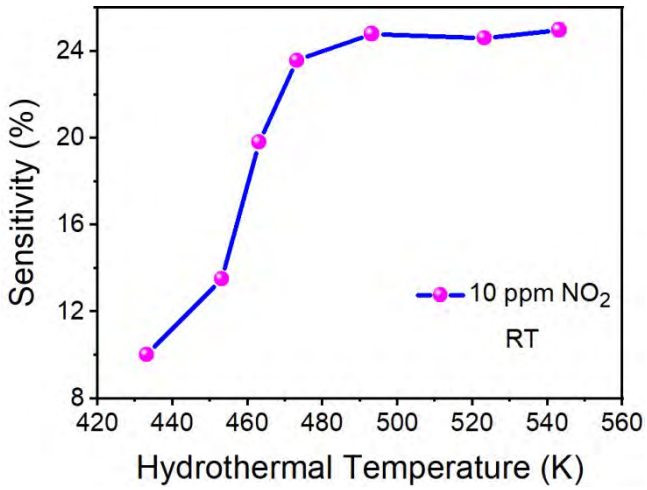

Figure S7. The room-temperature sensitivity of CeO_2/graphene composites toward 10 ppm NO_2 at different hydrothermal temperature.

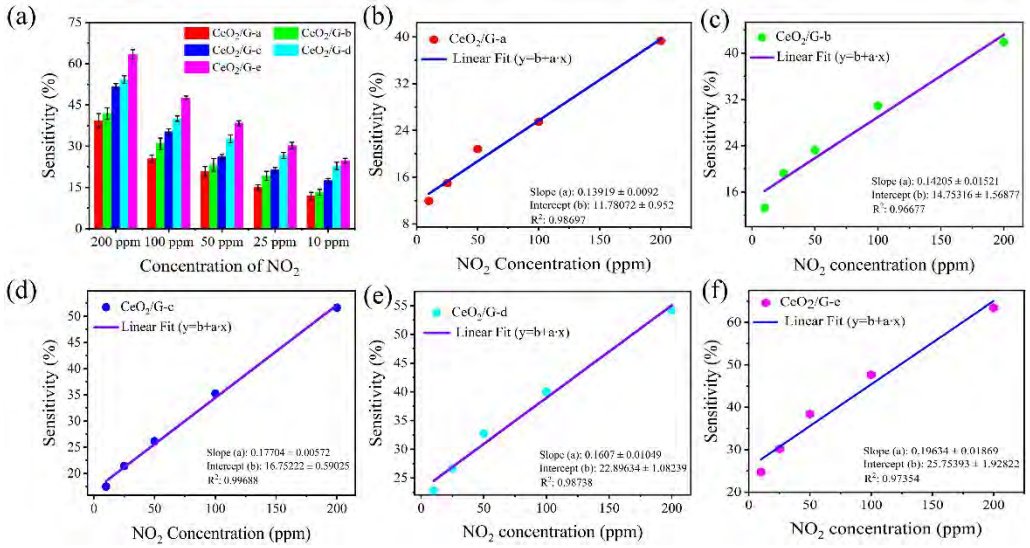

Figure S8. (a) The sensitivity of CeO_2/graphene composites toward 200 ppm, 100 ppm, 50 ppm, 25 ppm and 10 ppm NO_2 at RT. Fitting plots of CeO_2/G-a, CeO_2/G-b, CeO_2/G-c, CeO_2/G-d and CeO_2/G-e sensors.

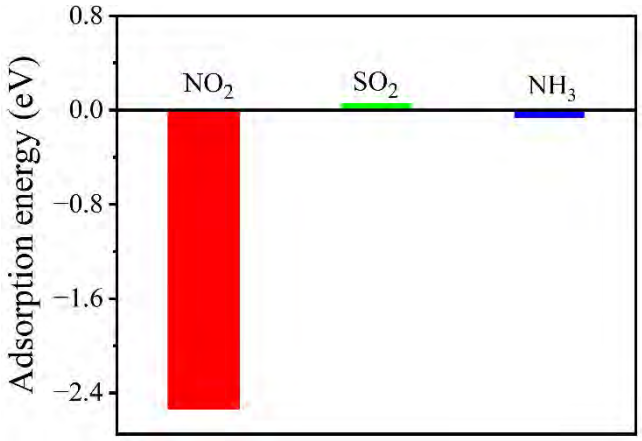

Figure S9. The adsorption energy of NO_2, SO_2 and NH_3 on the surface of CeO_2{100} facet.

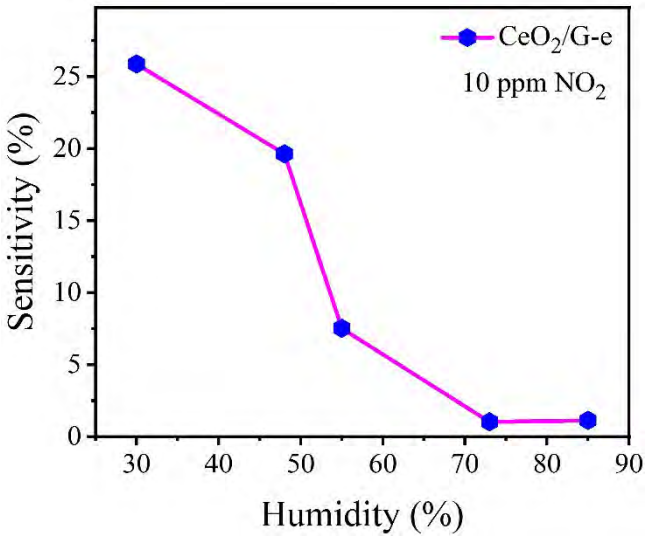

Figure S10. The room-temperature responses of the CeO_2/graphene composites toward 10 ppm of NO_2 at different humidity.

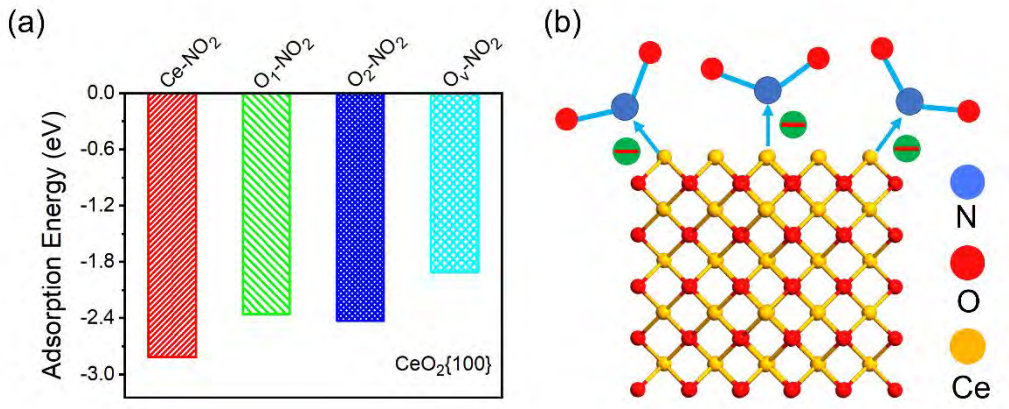

Figure S11. (a) Adsorption energy of NO_2 on the CeO_2{100} crystal plane and (b) Schematic illustration of NO_2 adsorption on the CeO_2{100} polar plane.

Table S1. The atomic ration of Ce, O and C elements.

The atomic ration	Ce	O	C
CeO_2/G-a	1	1.86	33.43
CeO_2/G-b	1	1.88	32.94
CeO_2/G-c	1	1.89	32.07
CeO_2/G-e	1	1.91	29.28

Table S2. Calculation of RMS noise and LOD for CeO_2/graphene composites sensors.

Sample	Slope (ppm^{-1})	Standard Error (ppm^{-1})	RMS	LOD (ppm)
CeO_2/G-a	0.13919	0.0092	0.158007	3.4
CeO_2/G-b	0.14205	0.01521	0.143051	3.02
CeO_2/G-c	0.17704	0.00572	0.1108656	1.87
CeO_2/G-d	0.1607	0.01049	0.081295	1.51
CeO_2/G-e	0.19634	0.01869	0.098693	1.5

In fact, the room-temperature sensing response is closely related to the external environmental factors, especially the environmental humidity. The H_2O molecule could react with oxygen ions on the surface of sensor and the less reactive hydroxyl groups (OH^-) is formed, decreasing the density of adsorption sites for NO_2 and behaving the poor gas sensing response. The concentration of water vapor in ambient air (25 ˚C) is 6280 ppm at the relative humidity of 20%. In addition, the water vapor concentration dynamically vary with change of the climate (wind, clouds, rainfall and so on), region, and season. Hence, the lower limit of detection can't be reached.

Table S3. Comparison of our proposed NO_2 sensor with recently reported other NO_2 sensor.

Materials	**Work temperature (℃)**	**Concentration (ppm)**	**Sensitivity (%)**	**Response /recovery time (s)**	**Reference**
SnO_2 nanobelt	400	0.5	15.5	120/360	[41]
WO_3	300	0.1	5.25	185/560	[42]
CeO_2 nanoparticles	100	40	54.54	240/438	[43]
CeO_2-Al_2O_3 nanocomposite	200	40	25	36/27	[44]
MoS_2	RT	5	15.2	245/ unrecoverable	[46]
Multilayer MoS_2	RT with UV light	5	17.9	29/260	[46]
Cu-MoS_2 composites	100	20	30	54/82	[47]
MoS_2-RGO composites	160	3	129	8/20	[48]
SnO_2/graphene composites	50	5	69.78	135/200	[12]
WO_3/RGO Composites	250	5	132	-/-	[13]
NiO/RGO Composites	200	5	82	-/-	[14]
CeO_2{111}/graphene composites	RT	100	10.39	7.33/150	[16]
CeO_2/graphene composites	RT with LED light	0.1	6	500/1	[18]
CeO_2/graphene composites	RT	5	63.63	320/1150	This work

(1) The sensing curves (reported for only one sample and one temperature Fig 8b are not good. They do not saturate and also the baseline is not fully recovered before the next pulse. I do think that these measurements do not support the conclusions of the authors.

Answer: Thanks for the reviewer's good suggestion. The sensing curves was measured again. The resistance is also not fully recovered to the original level before the next pulse. In fact, the gas sensing response is closely related to the external environmental factors (temperature, humidity, pressure and so on).The resistance would vary with the changes of external environment. Hence, the resistance is not fully recovered before the next pulse at some times. In addditon, except for the CeO_2/graphene composites in this paper, the MoS_2/graphene composites,[36] SnO_2/graphene composites,[50] CeO_2/graphene composites [18] and SnO_2/Ti_3C_2 composites [51] in the prevous work, the resistance is also not fully recovered to the original level before the next pulse (**Figure S12**). The thermal treatment and UV light irradiation were always used to enhance the rate of recovery.[18,51] Although, the baseline is not fully recovered before the next pulse, the NO_2-sensing response of all the samples were measured at the same external environmental factors. Hence, these measurements could support the conclusions in this paper.

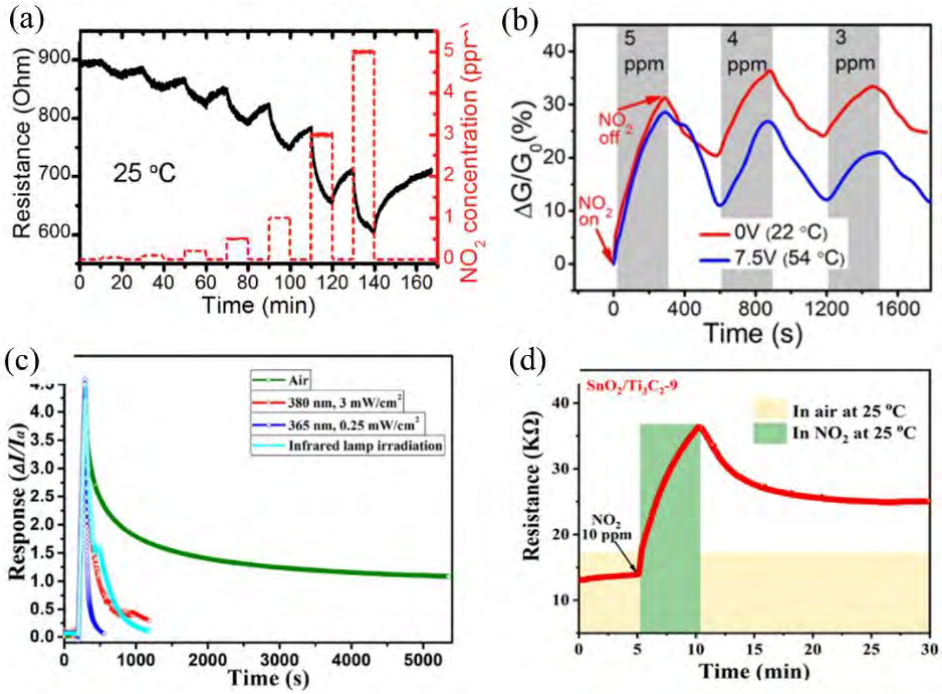

Figure S12. The response and recovery curves of (a) MoS_2/graphene composites,[36] (b) SnO_2/graphene composites,[50] (c) CeO_2/graphene composites [18] and (d) SnO_2/Ti_3C_2 composites [51] at RT, respectivily.

(2) Another aspect that has not been taken into consideration is the density of particles (i.e. the coverage) onto the reduced graphene oxide. Following the mechanistic studies of G. Neri and coworkers on CNTs and reduced graphene oxide coated with metal oxides, a continuous or almost continuous coating is required to create a transduction mechanism involving the metal oxide grain boundaries. In the present work the coating is not continuous (so RGO-RGO contacts can not be excluded) and it is also dependent on the particle size.

Answer: Thanks for the reviewer's good suggestion.The influence of density of CeO_2 particles onto the graphene on the room-temperature NO_2 sensing response was studied and the result was shown in the **Figure S13**. In this paper, the density of CeO_2 nanoparticles onto graphene was controlled by changeing the concentration of $Ce(NO)_3{\cdot}6H_2O$. The sensitivity of sensor toward 10 ppm NO_2 at RT is increased from 6.3% to 16.3% as the concentration of $Ce(NO)_3{\cdot}6H_2O$ was increased from 1.25 g/L to 3.75 g/L, After that value, the sensitivity was decreased. When introduction of low concentration of $Ce(NO)_3{\cdot}6H_2O$, tiny density of CeO_2 nanoparticles formed onto graphene. The higher quantity of graphene-graphene junctions are present and the electrical conduction flows mainly through the carbon-carbon contact. The adsorption energy of NO_2 on graphene was much lower than that on CeO_2[2]. Hence, the sensor behaves the poor NO_2-sensing response at RT. With increasing the concentration of $Ce(NO)_3{\cdot}6H_2O$, the density of CeO_2 particles on the graphene is increased. More CeO_2-graphene heterojunction is formed, behaving the better NO_2-sensing response. If further increasing the concentration of $Ce(NO)_3{\cdot}6H_2O$, the heterojunction are restricted mainly

to the interaction between CeO_2 nanoparticles and all the current flows through this pathway with high resistance, behaving the poor NO_2-sensing response.

In fact, the gas-sensing response of metal oxides are also affected by size of nanoparticles. The effect of size of CeO_2 nanoparticles on room-temperature NO_2 sensing response of CeO_2/graphene composites was studied in my previous work. The sensitivity of CeO_2/graphene composites toward 100 ppm NO_2 was increased from 16.83% to 32.7% as the size of CeO_2 nanoparticles was decreased from 20 nm to 3 nm. In essential, as the particle size is reduced, the fraction of surface atoms is increased and, the surface energy and surface tension increase resulting in more active surface atoms and more oxygen vacancies, accompanied by lattice strain, which is benefical to adsorption of NO_2 gas and thus displays the better NO_2-sensing response.

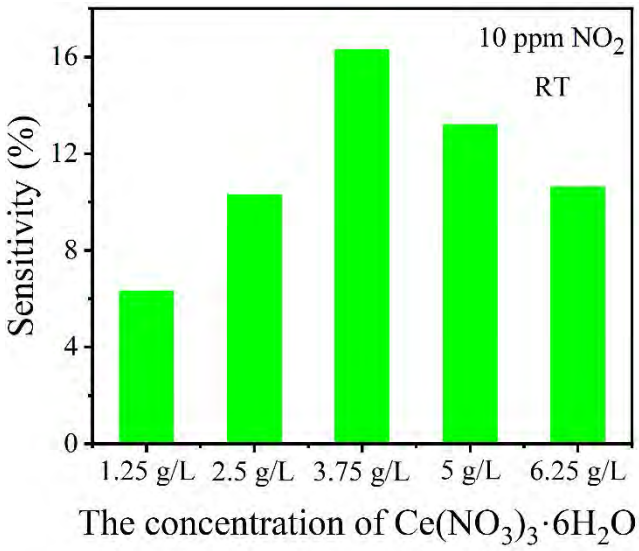

Figure S13. The sensitivity of CeO_2/graphene composites toward 10 ppm NO_2 at RT as the concentration of $Ce(NO_3)_3 \cdot 6H_2O$ is increased from 1.25 g/L to 6.25 g/L.

(3) How does the resistance of the CeO_2-graphene composites change when exposed to NO, NH_3, and CO?

Answer: Thanks for the review's good suggestion. The CeO_2/graphene composites are p-type semiconductors.[16] NO is the oxidizing gas, while NH_3 and CO is the reducing gas. Hence, the resistance is reduced when exposed to NO, but is increased when exposed to NH_3 and CO.[16]

(4) Where are the lattice stripes of GO in Figure 5?

Answer: As suggested by the reviewer, the TEM images of CeO_2/graphene composites were measured again. The lattice stripes of CeO_2 was obviously observed, while that of graphene was not observed for the CeO_2/graphene composites. To further characterize the graphene, the TEM images of prepared graphene were measured and the results were shown in **Figure S14**. It's obviously shown that the graphene displayed

the layer structure and contained fold. While, the lattice fringes of graphene was not obviously observed. In addition, for the SnO_2/graphene composites[S2] and ZnO/graphene composites [S3] in the previous work, the lattice stripes of graphene was also not observed.

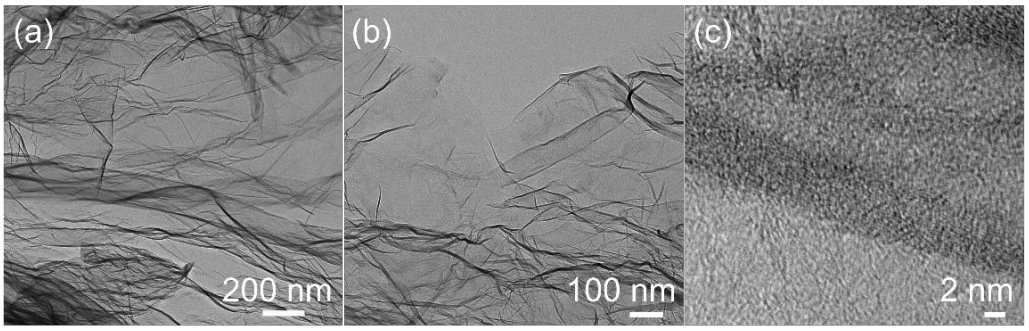

Figure S14. The (a, b) TEM and (c) HR-TEM images of graphene

[S2] Wang, Z. Y.; Han, T. Y.; Fei, T.; Liu, S.; Zhang T. Investigation of microstructure effect on NO_2 sensors based on SnO_2 nanoparticles/reduced graphene oxide hybrids. *ACS Appl. Mater. Interfaces* **2018**, *10*, 41773−41783.

[S3] Saranya, M.; Ramachandran, R.; Wang, F. Graphene-zinc oxide (G-ZnO) nanocomposite for electrochemical supercapacitor applications. *J. Sci.-Adv. Mater. Dev.* **2016**, *1*, 454−460.

(5) The sensing mechanism is too vague.

Answer: Thanks for the reviewer's good suggestion. We carefully read the section of sensing mechanism. In this paper, the composites of graphene and cubic CeO_2 nanoparticles with the exposed {100} facet are prepared hydrothermally. The percentage of high-energy {100} polar plane increases as the synthesis temperature is increased, while the those of Ce^{3+} and oxygen vacancy (O_v) decrease. As a result, the

room-temperature sensitivity of CeO_2{100}/graphene composites towards NO_2 is enhanced. According to the results of first-principles calculation, the adsorption energy of NO_2 on the 6-coordination Ce atoms is more negative and hence, adsorption of NO_2 is more favorable on the {100} polar plane of CeO_2. Moreover, when the proportion of O_v is reduced, the density of 6-coordination Ce atoms is improved. At the same time, the polarity of CeO_2{100} facet improves, and the interactions between NO_2 and the {100} facet are enhanced. As a result, the NO_2 sensing response on the CeO_2{100} facet is improved at room temperature. Hence, the mechanism of NO_2-sensing enhancement is clearly revealed by combining the experimental and theoretical studies in this paper. The sensing mechanism is not vague.